



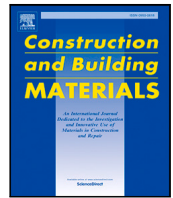
## **A two-stage study of steel corrosion and internal cracking revealed by multimodal tomography**

Downloaded from: <https://research.chalmers.se>, 2024-03-20 11:48 UTC

Citation for the original published paper (version of record):

Alhede, A., Dijkstra, J., Robuschi, S. et al (2023). A two-stage study of steel corrosion and internal cracking revealed by multimodal tomography. *Construction and Building Materials*, 394.  
<http://dx.doi.org/10.1016/j.conbuildmat.2023.132187>

N.B. When citing this work, cite the original published paper.



# A two-stage study of steel corrosion and internal cracking revealed by multimodal tomography

Andreas Alhede<sup>a,\*</sup>, Jelke Dijkstra<sup>a</sup>, Samanta Robuschi<sup>b</sup>, Alessandro Tengattini<sup>c</sup>, Karin Lundgren<sup>a</sup>

<sup>a</sup> Chalmers University of Technology, 412 96, Gothenburg, Sweden

<sup>b</sup> Norconsult AB, Gothenburg, Sweden

<sup>c</sup> Institut Laue-Langevin, Grenoble, France

## ARTICLE INFO

Dataset link: <https://doi.org/10.5291/ILL-DAT A.UGA-78>

### Keywords:

Neutron and X-ray Computed Tomography  
Corrosion  
Reinforced Concrete  
Multimodal Registration  
Digital Volume Correlation

## ABSTRACT

Modeling of corrosion-induced cracking is limited by lacking knowledge on the behavior of corrosion products. In this work, the corrosion and cracking processes were experimentally investigated in 3D at two different stages. The processes were measured at micro-structural scale, applying nondestructive neutron and X-ray computed tomography in two scans at different stages in the corrosion process. A method to evaluate the average volumetric strain of the compressed corrosion layer was proposed and displacements in the concrete matrix were measured. Strain localization revealed cracks not directly visible in the images. Multimodal tomography demonstrated to be an effective method for investigating steel corrosion in reinforced concrete.

## 1. Introduction

Corrosion of steel in concrete is the most common deterioration mechanism [1] for structures located in aggressive environments, e.g. structures in marine environments or structures exposed to deicing salts. Chlorides, when reaching the steel–concrete interface, depassivate the protective film that prevents the steel from corroding. Steel corrosion in reinforced concrete can also be induced by carbonation of the concrete [2]. When carbon dioxide diffuses into the pore network of the concrete, it reacts with the calcium hydroxide, subsequently lowering the pH of the pore solution. The carbonation front gradually penetrates through the concrete and when it reaches the level of the steel, depassivation takes place.

Oxidation of steel into corrosion products leads to a volume increase, but the concrete cover limits corrosion from expanding. Hence, a stress-dependent volume increase takes place, which leads to cracking of the concrete cover. Corrosion results in loss of the effective cross-sectional area of steel, reducing the load-bearing capacity, which ultimately can lead to failure of the structural element. In case of pitting corrosion, strain localization at the pits can result in a brittle failure [3] and a reduced fatigue performance [4]. Furthermore, steel corrosion and concrete cracking have a detrimental effect on the bond behavior, which influences the safety in anchorage regions [5].

Degradation of reinforced concrete due to steel corrosion is a complex phenomenon with a large number of influencing factors, e.g., geometry, concrete quality and exposure conditions. Important factors in modeling of the corrosion and cracking processes include parameters related to corrosion products, such as the volume expansion and the constitutive relation between compressive stress and strain. Further, parameters more related to the concrete, for example the ability of concrete to accommodate corrosion products in vicinity of the steel–concrete interface (the corrosion accommodating region [6]) and transport of corrosion products through the pore network and cracks [7] are considered important. Model parameters associated to the corrosion and cracking processes are difficult to quantify with traditional destructive techniques, e.g. due to immediate changes in chemical composition when corrosion products are exposed to a high content of oxygen [8], as in atmospheric conditions. Prior experimental research has therefore focused on relations between surface crack width and internal corrosion damage [9–16]. Several models (for example [17–23]) have been proposed, in which the above mentioned parameters have been calibrated by fitting with the measured surface crack width, crack pattern, and final corrosion level. The huge scatter in experimental results (e.g. Andrade [12], Tahershamsi [15]) indicates that fitting micro-structural parameters, that govern the corrosion process on the interface between the bar and the concrete, such as the

\* Corresponding author.

E-mail address: [andreas.alhede@chalmers.se](mailto:andreas.alhede@chalmers.se) (A. Alhede).

<https://doi.org/10.1016/j.conbuildmat.2023.132187>

Received 13 February 2023; Received in revised form 14 June 2023; Accepted 15 June 2023

Available online 28 June 2023

0950-0618/© 2023 The Author(s). Published by Elsevier Ltd. This is an open access article under the CC BY license (<http://creativecommons.org/licenses/by/4.0/>).

corrosion level, with results at the boundary value level (crack width) is insufficient. This leads to parameter sets that are non-unique and dependent on the experimental data against which they are fitted.

There is an urgent need for an experimental approach to characterize corrosion within the reinforced structure without changing the environment corrosion products are exposed to. Nondestructive methods, providing noninvasive data from the inside of specimens, have shown to be very promising tools [24]. For example, in [25], the presence of concrete cracks was found to influence the formation of corrosion products. Corrosion was observed to be more pronounced around the perimeter of the steel near concrete cracks, while less corrosion occurred in uncracked regions. Additionally, in [26], it was demonstrated how the evolution of steel corrosion could be investigated by time-resolved micro X-ray Computed Tomography (CT).

The purpose of this work is to assess to what extent combined time-resolved neutron and X-ray imaging can contribute to the calibration of micro-structural parameters in corrosion models by linking corrosion characteristics and kinematics during corrosion propagation. This paper utilizes combined neutron and X-ray CT, exploiting the two different contrast mechanisms offered by attenuation of neutrons and X-rays within the material, allowing for complementary information within the sample. X-ray attenuation is sensitive to the atomic number of the material [27] and density changes in the sample, which allows for distinguishing air voids, steel and the concrete matrix. Neutrons, on the other hand, interact with the nuclei of the atoms [28], and are sensitive to light elements such as hydrogen and thus to cement paste and corrosion products. A previous study employed multimodal neutron and X-ray CT to characterize steel corrosion in specimens taken from an engineering concrete structure [29]. This approach has also been used to investigate the impact of air voids at the steel–concrete interface on corrosion initiation [30]. The aim of this work is instead to examine how changes in material phases within the sample can be used to estimate the volumetric strain of compressed corrosion. In addition, this study also aims to measure corrosion-induced deformations in the concrete matrix and qualitatively compare these deformations with the local corrosion level and concrete cracking.

## 2. Method

One reinforced concrete specimen was cast, cured and subjected to accelerated corrosion. Thereafter, neutron and X-ray CT were acquired after two different periods of corrosion propagation. From the CT data, a phase segmentation analysis and Digital Volume Correlation (DVC), respectively, were carried out. The former was used to compute the local corrosion level along the length of the bar, and to quantify input parameters for a derived expression to calculate the average volumetric strain in the compressed corrosion layer. The latter of these analyses was used to measure corrosion-induced deformations within the concrete matrix.

### 2.1. Materials & specimen preparation

One cylindrical reinforced concrete specimen was cast in the laboratory. The specimen, illustrated in Fig. 1a, had a diameter of 150 mm and a length of 130 mm. The reinforcement bar used, a plain reinforcement bar with a nominal diameter of 16 mm, was extracted from a bridge built in Gullspång, Sweden in 1935 [31], and was selected due to its minimal initial damage. The bar was sandblasted to remove cement paste and small fragments of corrosion products. The yield stress of 27 uncorroded bars, extracted from the same bridge, was measured [31]. The average yield stress was 259.6 MPa, with a standard deviation of 10.1 MPa. A portable scanner [32] was used to characterize the surface area of the steel before casting the specimen.

The concrete was cast with cement type CEM I 42.5R [33] and a water–cement ratio of 0.47. Superplasticizer was added to the concrete mix to improve the workability. The consistency of the fresh concrete

**Table 1**

Concrete mix proportions.

|  |       |
|--|-------|
| Water [kg m <sup>-3</sup> ]                | 171.6 |
| Cement [kg m <sup>-3</sup> ]               | 365.0 |
| Sand (0/4 mm) [kg m <sup>-3</sup> ]        | 943.0 |
| Aggregates (4/16 mm) [kg m <sup>-3</sup> ] | 911.0 |
| Superplasticizer [% by mass of cement]     | 1     |
| Sodium chloride [% by mass of concrete]    | 4     |

was liquid without segregation. Sodium chloride was added to the concrete mix to prevent the formation of a passive layer around the steel. The concrete composition is specified in Table 1. Following a 28-day period of concrete curing, the compressive and tensile strength of the concrete were subsequently measured. The compressive strength of three concrete cylinders, each with a diameter of 100 mm and a length of 200 mm, was measured following the guidelines specified in [34]. The mean compressive strength was determined to be 59.5 MPa. The tensile strength of three concrete cylinders was measured from uniaxial tensile tests following the guidelines in [35]. Each cylinder had a diameter of 100 mm and a length of 100 mm. Prior to conducting the test, a notch with dimensions 3 mm in width and 15 mm in depth, was carefully cut in the middle of the specimens. The mean tensile strength was measured to 3.3 MPa, while the mean fracture energy was measured to 175 N m/m<sup>2</sup>.

Accelerated corrosion was imposed through impressed electrical current at two different phases, prior to the imaging experiment (phase one) and at the neutron facility after the first scan was completed (phase two). Corrosion was achieved by submerging the specimen in its upright position in a container filled with saline water (5% sodium chlorides). In phase one, a current density ( $I_{\text{corr}}$ ) of 100  $\mu\text{A cm}^{-2}$  was applied for 31 days (Fig. 1a) and corrosion-induced cracks could be observed with the naked eye. After this first period, a specimen with a smaller section was cored out (Fig. 1b) to obtain higher spatial resolution of the tomographies by reducing the required field of view. The sample was also dried at a temperature of 85 °C for a period of three hours to improve the quality of the neutron tomographies.

Subsequently, the first tomography scan was carried out, with the acquisition parameters detailed in Section 2.2. After the first scan, the corrosion level was increased further. In phase 2, the current density was significantly higher, 2985  $\mu\text{A cm}^{-2}$ , and applied for a shorter duration. The high current density was chosen to allow sufficient corrosion propagation in a limited period of time, as the second scan had to be executed the second day of the allotted beamtime. In this phase, the impressed current was too high to directly represent natural corrosion [11,36]. However, the main aim was in fact not to mimic natural corrosion but to evaluate how multimodal neutron and X-ray imaging could be used to estimate the volumetric strain of compressed corrosion and to measure corrosion-induced deformations in the concrete matrix.

### 2.2. Neutron and X-ray computed tomography

The NeXT neutron and X-ray tomograph at the Institute Laue-Langevin [37] was used to acquire the tomographies of the specimen. Two scans, one prior and one after additional corrosion, were performed. Details on the imaging acquisition are summarized in Table 2.

The two tomographies were acquired at slightly different resolutions/field of view and in slightly different areas. The Region of Interest (ROI) for this work is the region where the volumes overlapped, ROI  $\in$  Scan 1  $\cap$  Scan 2 (Fig. 1c). A Feldkamp filtered back-projection algorithm [38] was used to reconstruct the neutron and X-ray projections into 3D tomographies. Fig. 2 shows slices of the specimen as obtained from X-ray and neutron CT, respectively. Four separate datasets were acquired during the experiment.

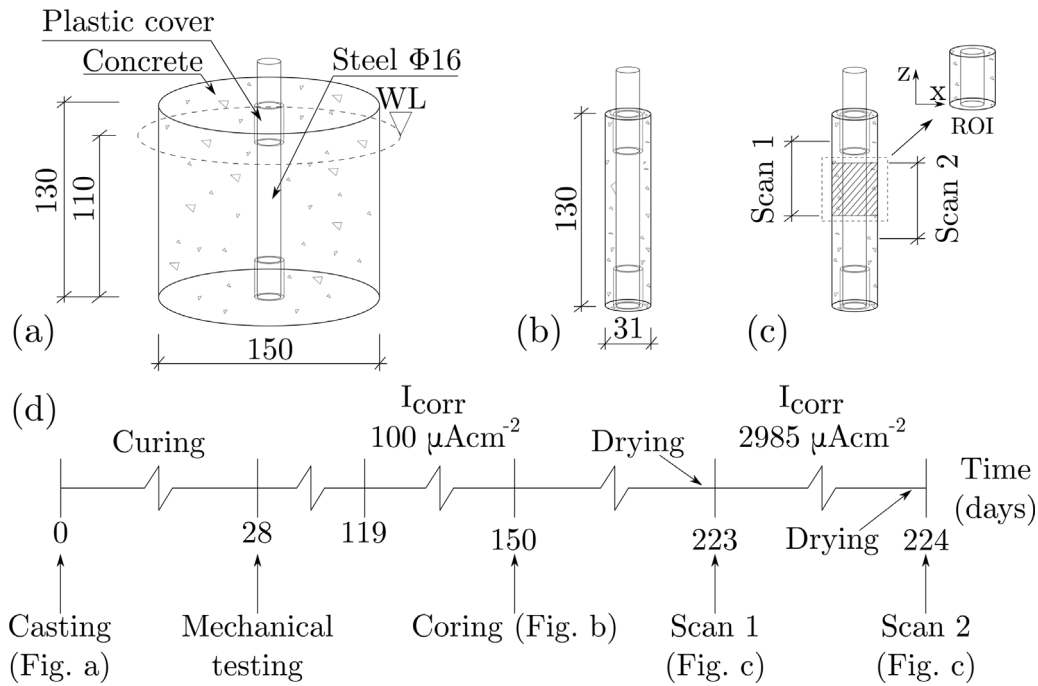


**Fig. 1.** Technical details of specimen and timeline. Measures in millimeter. Top: Geometry of specimen at different stages. (a) Initial geometry at casting and first corrosion propagation period, including water level (WL) for the galvanic cell. (b) Geometry of specimen for Scan 1 and 2, and for the second corrosion propagation period. (c) Scanned parts of the specimen, including Region of Interest (ROI). (d) Timeline.

**Table 2**

Data acquisition for neutron and X-ray computed tomography.

|  | Neutrons |        | X-rays |        |
|--|----------|--------|--------|--------|
|  | Scan 1   | Scan 2 | Scan 1 | Scan 2 |
| Nominal voxel size [ $\mu m px^{-1}$ ] | 26       | 26     | 36     | 36     |
| Number of projections                  | 1850     | 1869   | 1900   | 1900   |
| Voltage [kV]                           | –        | –      | 140    | 140    |
| Current [ $\mu A$ ]                    | –        | –      | 214    | 214    |
| Frame rate [ $s^{-1}$ ]                | –        | –      | 5      | 5      |
| Exposure time [s]                      | 2.75     | 2.75   | –      | –      |
| Field of view [mm]                     | 65       | 65     | –      | –      |

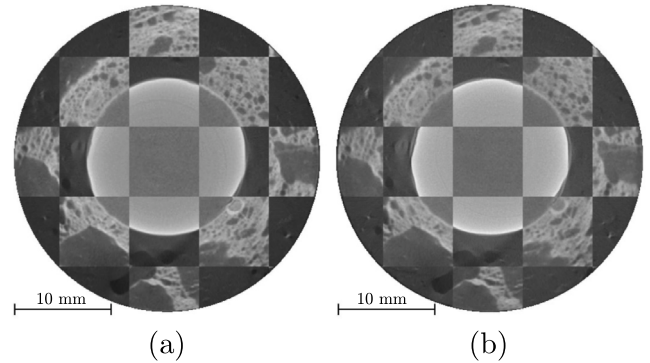


**Fig. 3.** A cross-sectional slice of combined neutron and X-ray data after image registration. (a) Scan 1 (b) Scan 2.

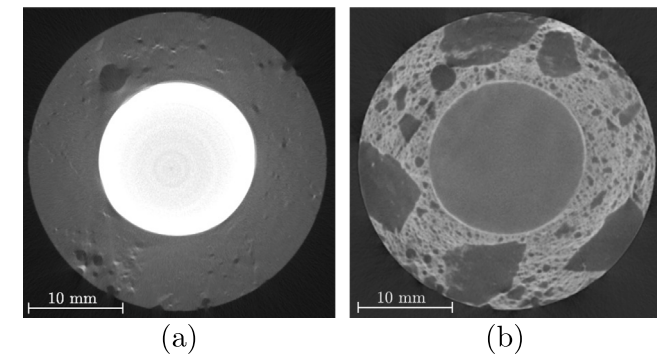


**Fig. 2.** A cross-sectional slice of the sample obtained from Scan 1, shown by (a) X-ray CT and (b) neutron CT.

### 2.3. Multimodal registration and image segmentation

Imaging datasets acquired from different imaging techniques have different information, and a multimodal registration is a necessary step to fully exploit the high complementarity of this information [39]. In the experiment presented here, the X-ray attenuation fields resolve the voids in the concrete matrix and the reinforcing steel. In contrast, the attenuation fields from the neutron scans enable the separation of the

cement matrix from the aggregates, due to its higher moisture content. Corrosion products, which are also hydrogen rich, can also be identified from the attenuation of neutrons.

The multimodal registration requires, as a first step, a statistical joint distribution of absorption coefficients to be analyzed. The datasets were registered by steps in the 3D space, thus including translations, rotations and scaling. First, an eye registration was performed to initially align the datasets. Second, the neutron dataset was registered on the X-ray dataset for Scans 1 and 2, respectively. The finer registration was performed by iteratively computing a linear transformation matrix [40]. An example of this alignment is shown in Fig. 3. Third, the datasets obtained from Scan 1 were registered on datasets obtained from Scan 2. After registration, a multivariate (joint) histogram was constructed to study the mutual information between the different modalities neutron and X-ray imaging datasets. The mutual information was computed by counting the occurrence of combinations of a pair of grayvalues. Two normalized joint histograms are shown in Fig. 4 for the cross-sectional slices illustrated in Fig. 3. The normalized histograms of the attenuation coefficients obtained from the individual X-ray and

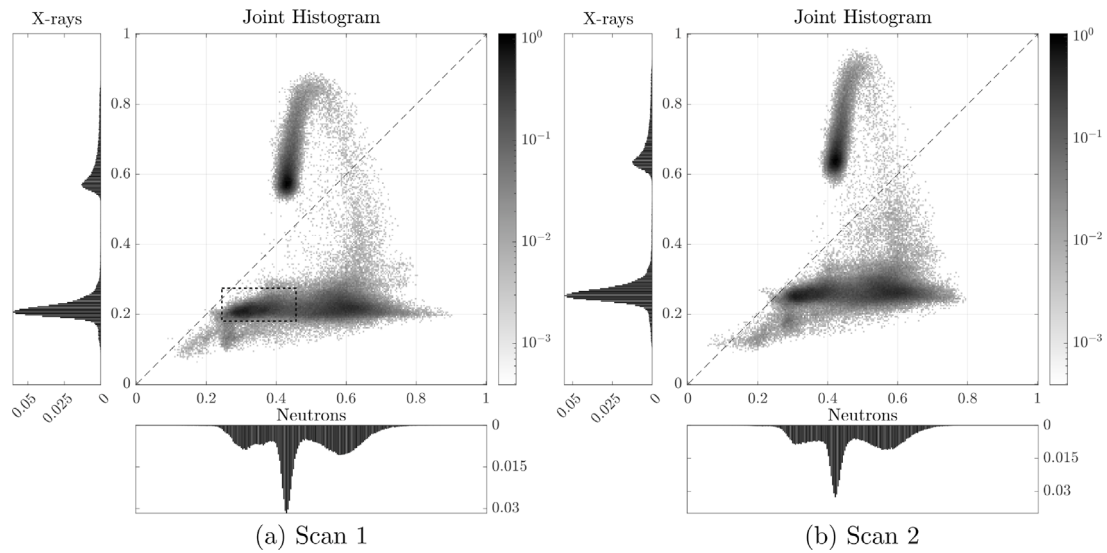


**Fig. 4.** Normalized joint histograms and individual histograms for X-rays and neutrons, for the cross-sections in Fig. 3, illustrating the grayscale correspondences. Larger intensities indicate a larger correspondence between the datasets. The rectangle in the joint histogram in (a) represents the region defining aggregates, as an example of how phase segmentation was carried out.

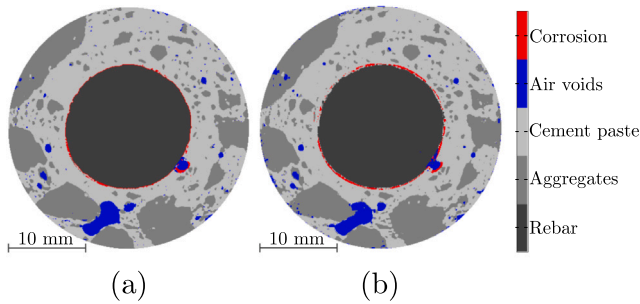


**Fig. 5.** A phase-segmented cross-sectional slice. (a) Scan 1 (b) Scan 2. (For interpretation of the references to color in this figure legend, the reader is referred to the web version of this article.)

neutron datasets are also added to simplify the visual interpretation of the multidimensional distributions. Two distinct peaks corresponding to the concrete and steel, respectively, can be observed in the X-ray histograms (compare with Fig. 2a). The distribution of attenuation coefficients in the neutron histograms is more uniform and concentrated to the region 0.2 to 0.7, with a peak around 0.42.

Subsequently, four material phases were identified with a sufficient fidelity based on the joint histogram: aggregates, cement paste, air voids and steel. Table 3 presents the ranges of normalized grayvalues for both modalities used for phase segmentation. An example is given in Fig. 4a, where the rectangle highlights the values for the aggregates in Scan 1. The determination of the grayvalue ranges for each material phase involved an iterative process, where the identified material phases were compared to the residual field of the imaging datasets. It was assumed that the noise in the joint histograms shown in Fig. 4 was influenced by the partial volume effect [41], which limited the identification of individual voxels.

Due to the large contrast in material densities within the sample, the X-ray data was affected by beam hardening. Beam hardening is an artifact that occurs when low-energy X-rays are absorbed or scattered more than high-energy X-rays, resulting in an increased mean energy of the X-ray beam [42]. This artifact makes the edges of the material more attenuating (brighter) than the remaining material. This was in particular the case for the steel, which hampered the interpretation at the steel–concrete interface. Hence, corrosion products were identified

**Table 3**

Combination of normalized grayvalues used for phase segmentation.

|              | Neutrons    |             | X-rays      |             |
|--------------|-------------|-------------|-------------|-------------|
|              | Scan 1      | Scan 2      | Scan 1      | Scan 2      |
| Aggregates   | 0.244–0.456 | 0.263–0.442 | 0.180–0.274 | 0.227–0.288 |
| Cement paste | 0.456–0.670 | 0.442–0.660 | 0.180–0.280 | 0.227–0.317 |
| Air voids    | 0.10–0.31   | 0.10–0.32   | 0.10–0.180  | 0.10–0.227  |
| Steel        | 0.400–0.463 | 0.400–0.456 | 0.550–0.800 | 0.590–0.864 |

separately from the neutron data. An example of phase segmented images is shown in Fig. 5.

#### 2.4. Local corrosion level

The local corrosion level was estimated based on the ratio between the corroded cross-sectional area of the steel bar ( $A_{sc}$ ) and the uncorroded one ( $A_{s0}$ ), estimated as the average cross-sectional area of the initial steel bar, as obtained from the 3D scanning detailed in Section 2.1.

$$C_l = 1 - \frac{A_{sc}}{A_{s0}} \quad (1)$$

#### 2.5. Average volumetric strain of compressed corrosion products from measurements

To evaluate the mechanical properties of corrosion products, the average volumetric strain in the compressed corrosion layer is of interest. In the following, it is shown how this can be evaluated from the evolution of material phases, by assuming that the decrease in air void volume is filled with uncompressed corrosion products, thus

$$V_{ca} = V_{a0} - V_a \quad (2)$$

where  $V_{ca}$  is the volume of the uncompressed corrosion products in the air voids,  $V_a$  is the volume of the air voids, and  $V_{a0}$  is the volume of the air voids before corrosion started. Further, the volume of the compressed corrosion products,  $V_{cc}$ , can be calculated as

$$V_{cc} = V_c - V_{ca} \quad (3)$$

where  $V_c$  is the total volume of the corrosion products. Then, the average volumetric strain in the compressed corrosion layer becomes

$$\varepsilon_v = \frac{V_{cc}}{\eta \Delta V_s - V_{ca}} - 1 \quad (4)$$



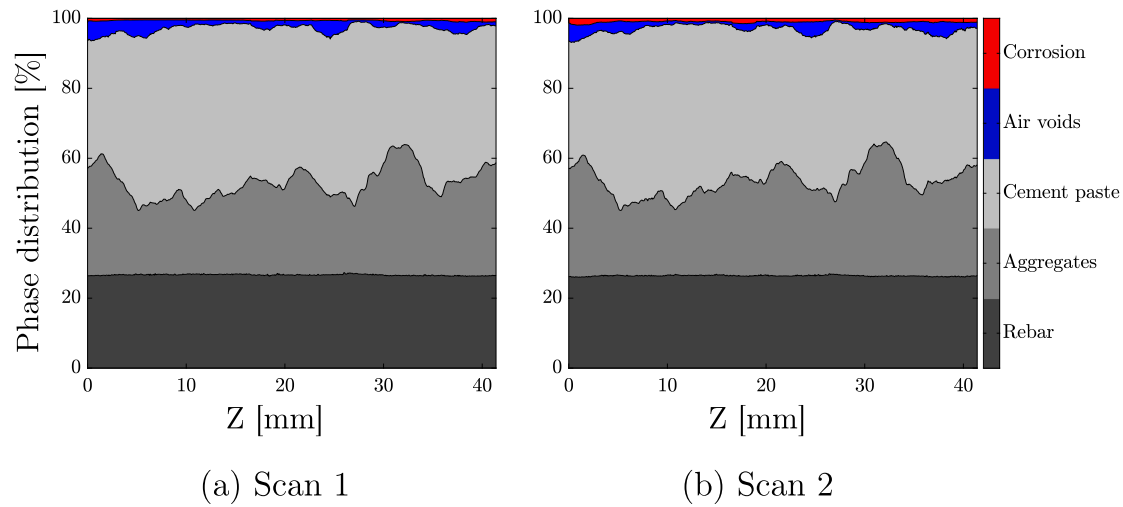


Fig. 6. Distribution of material phases along the length (Z) of the specimen. (For interpretation of the references to color in this figure legend, the reader is referred to the web version of this article.)

where  $\eta$  is the iron to rust volumetric ratio. This was in earlier work evaluated from the measured volume of corrosion products in macroscopic interfacial voids and the loss of steel in the corresponding corrosion pit [29]. The volume of the steel loss,  $\Delta V_s$ , can be calculated as

$$\Delta V_s = V_{s0} - V_s, \quad (5)$$

where  $V_s$  is the volume of the steel and  $V_{s0}$  is the volume of the steel before corrosion started. The nominator in Eq. (4) can be recognized as the volume of the compacted corrosion products if it was free to expand.

## 2.6. Digital volume correlation

A local DVC [40] was conducted to measure corrosion-induced deformations within the concrete. For this analysis, the neutron datasets were used, because of their higher contrast (compared to the X-ray datasets). Similar to the multimodal registration, an image registration was carried out to align the two datasets to compensate for the different placement of the sample during scanning. Subsequently, a local DVC was carried out.

The datasets were divided into cubic subvolumes where the size was refined iteratively, starting from a coarse size. The final cubic size was 0.75 mm and was considered acceptable based on the number of successfully correlated subvolumes (97.5%). One node was assigned at the center of each subvolume, for which the local displacement was computed. The steel was masked in the image data by thresholding the grayvalues, due to the low spatial contrast. Rigid body motions, obtained from image registration, were subtracted from the displacement field. The remaining part of the displacement field was therefore assumed to represent the physically relevant deformations.

Prior to the strain calculation, the displacement field was corrected for poorly correlated subvolumes using the methodology elaborated in Appendix.

## 3. Results and discussion

### 3.1. Spatial distribution and corrosion

The total distribution of the main material phases were summed for all cross-sectional slices of the specimen and is illustrated in Fig. 6 as a function of the length of the specimen. For Scan 1, the proportion of corrosion products is nearly uniform along the length of the specimen, even though some local regions show more corrosion. For Scan 2, the amount of corrosion increased whilst simultaneously the amount of air

Table 4

Volume of corrosion products, air voids and steel.

| Volume of:                                   | Scan 1 | Scan 2 | $\Delta V$ |
|--|--------|--------|------------|
| Corrosion products [mm <sup>3</sup> ], $V_c$ | 200.2  | 331.2  | 131        |
| Air voids [mm <sup>3</sup> ], $V_a$          | 721.7  | 653.0  | -68.7      |
| Steel <sup>a</sup> [mm <sup>3</sup> ], $V_s$ | 8480.0 | 8404.4 | -75.6      |

<sup>a</sup>The volume of the steel before corrosion started was  $V_{s0} = 8626.7 \text{ mm}^3$ .

voids decreased. In Table 4, the volumes of corrosion products, air voids and steel are summarized. As expected, for Scan 2, the volume of steel decreased whilst the volume of corrosion products increased. The volume of air voids decreased, indicating that corrosion products occupy the void space close to the steel. This phenomenon can also be observed in Fig. 5.

The loss of steel from corrosion propagation between the scans is presented in Fig. 7, where the change in the radius of the bar,  $\Delta r$ , is plotted as function of the radial and longitudinal directions. This figure also shows the increase in local corrosion level,  $\Delta C_l$ , between the scans. The contour plot indicates a relatively uniform steel loss that is consistent with the results in [43], where the distribution of corrosion products along the bar became more uniform when a high current density was applied. However, one larger corrosion pit can be observed in the region  $0 \leq Z \leq 5 \text{ mm}$ .

### 3.2. Estimation of the average volumetric strain of compressed corrosion products

As described in Section 2.5, the average volumetric strain of compressed corrosion products can be calculated from the evolution of material phases. From the measurements in this experiment,  $V_c$ ,  $V_a$ ,  $V_s$  and  $V_{s0}$  are known, while the volume of the air voids before corrosion starts ( $V_{a0}$ ) is unknown, as no scanning was performed before corrosion started. Yet, the differences between Scans 1 and 2 can be treated in an analogous way as described in Section 2.5. By use of the values listed in Table 4, the average volumetric strain of compressed corrosion at Scan 2 can be calculated as a function of the free volumetric expansion coefficient of corrosion products. The results are shown in Fig. 8. The relationship between volumetric strain and volumetric expansion coefficient demonstrates nonlinearity, with strain values approaching zero when the volumetric expansion coefficient is small, i.e. when the denominator in Eq. (4) approaches zero. As an example, assuming the volumetric expansion coefficient to be  $\eta = 3.91$ , as evaluated for accelerated corrosion in [29], which correlates well to the measures

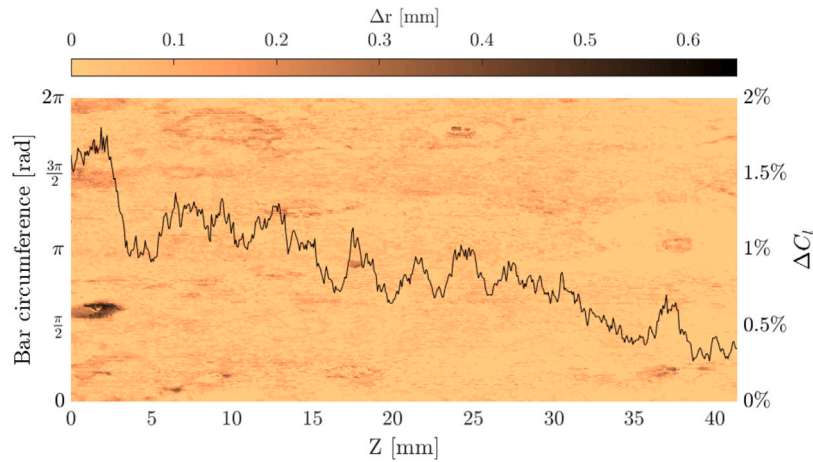


Fig. 7. Surface plot representing the reduction in steel bar radius,  $\Delta r$ , combined with the increase in local corrosion level between Scans 1 & 2,  $\Delta C_i$ , along the length (Z) of the specimen. (For interpretation of the references to color in this figure legend, the reader is referred to the web version of this article.)

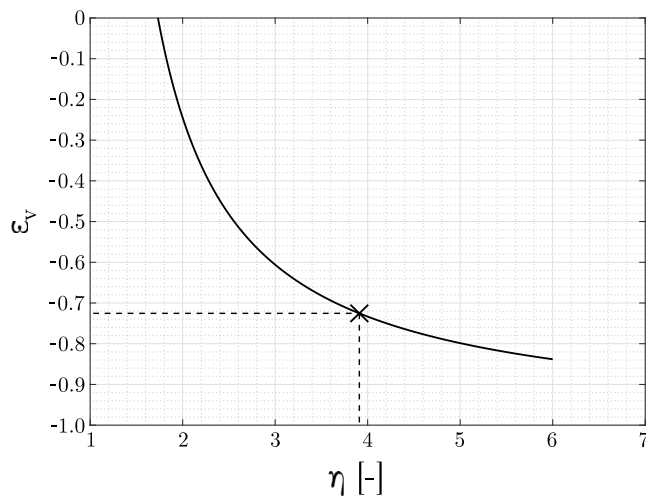


Fig. 8. Average volumetric strain,  $\epsilon_v$ , in the compressed corrosion layer as a function of the volumetric expansion coefficient  $\eta$ .

in [44,45], an average volumetric strain of the compressed corrosion at Scan 2 can be calculated to  $\epsilon_v = -0.72$ . Although the strain appears to be large, the magnitude is in close agreement with those measured in [46], for stress levels of reasonable magnitude. Moreover, the magnitude of the average volumetric strain of the compressed corrosion is not unreasonable, considering the large values for the iron to rust volumetric ratio applied.

### 3.3. Concrete cracking and kinematics

The displacement field extracted from DVC is plotted as a 3D vector plot in Fig. 9a). As can be seen, the displacements are non-uniform, with the largest displacements observed at the top part of the studied part of the specimen. In this area, a crack is clearly visible 27 mm from the boundary and onwards. Fig. 9b) represents the local corrosion levels along the length of the specimen. The area shaded in dark brown corresponds to the local corrosion level at Scan 1 and the area shaded in light brown corresponds to the additional local corrosion level developed between Scans 1 & 2. The local corrosion level at Scan 1 is higher in the region where the crack is identified.

To further investigate the role of cracks, Fig. 10 (top) reports three cross-sectional slices, selected as representative of areas where

cracks opened, of the neutron dataset from Scan 2. Locations are indicated in Fig. 9. An image overlay highlighting corrosion products (brown) and cracks (red) has been added. Cracks cannot be identified in cross-section A–A, but are partly visible in cross-section B–B. For cross-section C–C, the width of the two cracks, however, is sufficiently large to be fully visible from the image. Notably, one crack propagated through a single coarse aggregate. The same observation was documented in [29], and could possibly be attributed to the presence of low-strength aggregates. Beneath each slice, the corresponding map of the first principal strains, obtained from the image correlation, is shown. These maps exhibit a spatial resolution of 0.75 mm. As can be seen for cross-section C–C, strain localizes in the correspondence to the cracks. The strain maps of the other two cross-sections show the strain localization and are thus capable of detecting cracks that are invisible from a direct inspection of the image data.

## 4. Conclusions and outlook

The potential of combined neutron and X-ray Computed Tomography (CT) to monitor the evolution of steel corrosion in small-scale reinforced concrete was investigated. Specifically, the aim of the present research was to estimate the volumetric strain of compressed corrosion and to measure corrosion-induced deformations in the concrete matrix. The former was estimated by conducting multimodal neutron and X-ray CT analysis of the material phases in the sample. The latter was computed from two subsequent neutron datasets using Digital Volume Correlation.

The following conclusions were drawn:

- Combining time-resolved neutron and X-ray CT is a powerful method for phase segmentation, allowing the nondestructive monitoring of corrosion at the micro-structural scale.
- Corrosion products were accommodated in air voids located near the steel which decreased the pore volume.
- Using the volumes of corrosion products, air voids and steel measured from several subsequent scans, the average volumetric strain in the compressed corrosion layer can be calculated.
- The distribution of strains in the concrete was successfully quantified using local DVC. Even in regions where the crack was not visible, strain localization was captured through local DVC; thus, the kinematics of the early stages of crack propagation can be monitored.

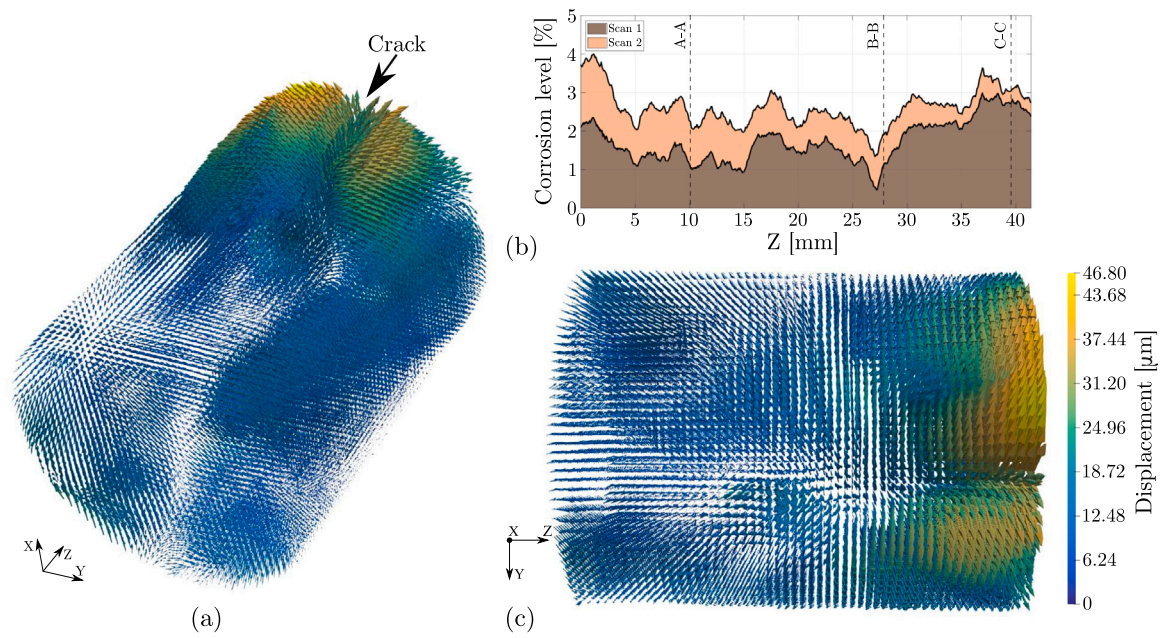


**Fig. 9.** (a) Displacement field within the concrete. (b) Local corrosion level along the length of the specimen at each scan. (c) Displacement field within the concrete. (For interpretation of the references to color in this figure legend, the reader is referred to the web version of this article.)

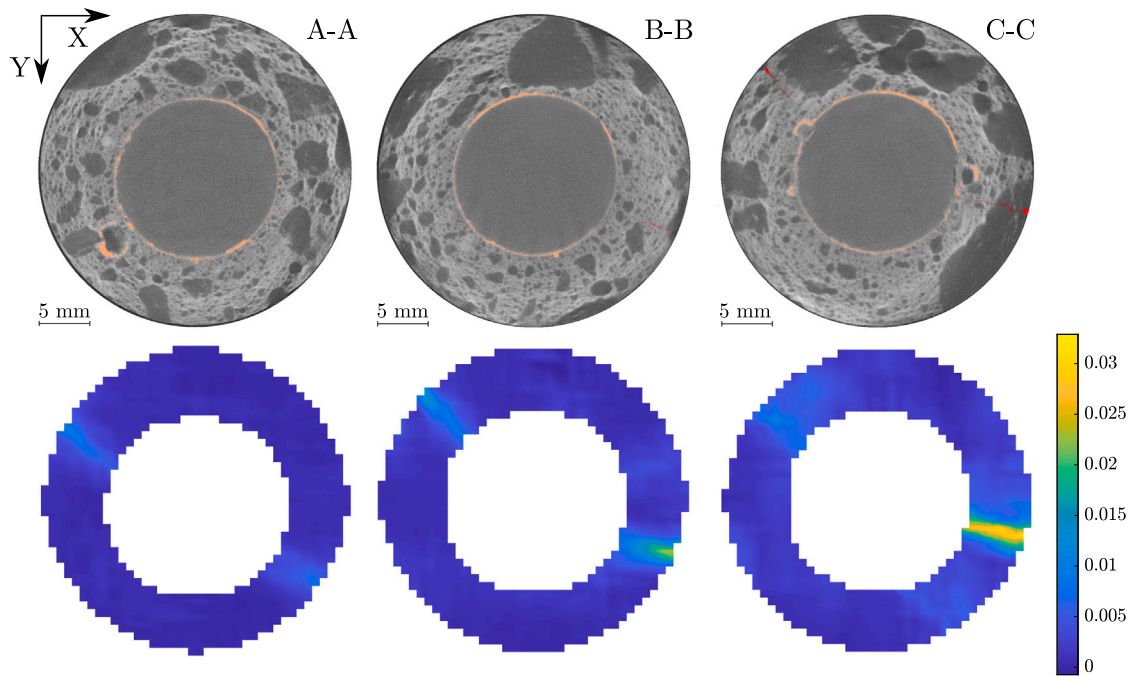


**Fig. 10.** Top row: Cross-sections of the specimen at three longitudinal positions, indicated in Fig. 9b. Image overlay highlights corrosion products (brown) and corrosion cracks (red). Bottom row: Corresponding map of the first principal strain. (For interpretation of the references to color in this figure legend, the reader is referred to the web version of this article.)



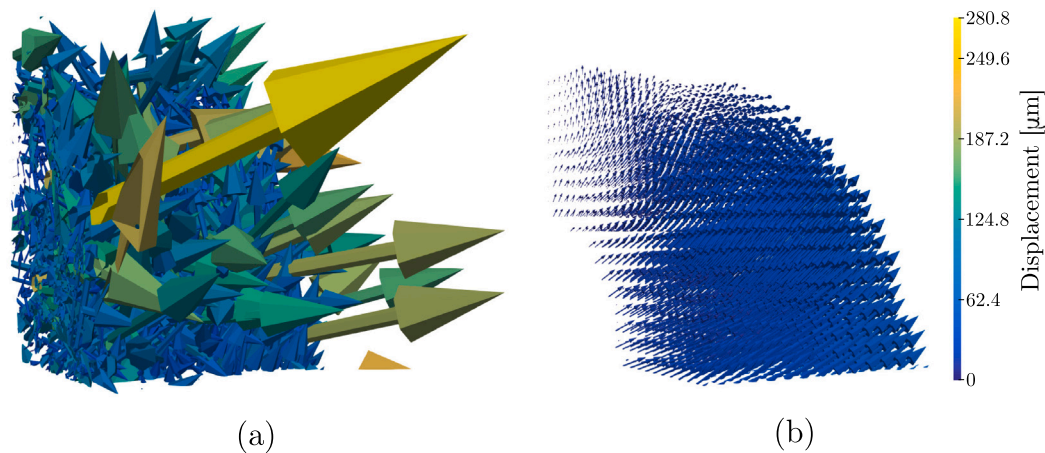


**Fig. A.11.** Displacements within a segment of the concrete cover obtained from a local DVC. (a) Displacements obtained after correction of badly correlated subvolumes. (b) Displacement field after filtering. (For interpretation of the references to color in this figure legend, the reader is referred to the web version of this article.)

It is important to note that the conclusions drawn from this exploratory test, presented here, were obtained as part of an experimental campaign involving post-mortem analyses of one artificially corroded reinforced concrete sample. Therefore, further research is needed to be able to validate and extrapolate these results to engineering structures. A natural progression of the current work is to design a dedicated test series for tracking the corrosion process within the sample and linking those with the kinematics, starting at the uncorroded state followed by several intermediate states of repetitive corrosion propagation.

#### CRediT authorship contribution statement

**Andreas Alhede:** Conceptualization, Data curation, Formal analysis, Visualization, Writing – original draft. **Jelke Dijkstra:** Conceptualization, Funding acquisition, Supervision, Writing – review & editing. **Samanta Robuschi:** Conceptualization, Investigation, Writing – review & editing. **Alessandro Tengattini:** Investigation, Writing – review & editing. **Karin Lundgren:** Conceptualization, Funding acquisition, Supervision, Writing – review & editing.

#### Declaration of competing interest

The authors declare that they have no known competing financial interests or personal relationships that could have appeared to influence the work reported in this paper.

#### Data availability

The data used in this study are made available at <https://doi.org/10.5291/ILL-DATA.UGA-78>.

#### Acknowledgments

The authors would like to acknowledge the ILL for granting the possibility to carry out the experimental work at the D50T instrument (research proposal UGA-78). The computations were enabled by resources provided by the Swedish National Infrastructure for Computing (SNIC) at Chalmers e-Commons, partially funded by the Swedish Research Council through grant agreement no. 2018-05973.

#### Funding

This project was financially supported by the Swedish Research Council Formas (grant no. 2019-00497) and the Swedish Transport Administration (grant no. 2021/27819).

#### Appendix. Filtering of displacement field

Converged correlations from the local DVC were reached for 97.5% of all subvolumes. For badly correlated subvolumes, displacements were corrected (replaced) prior to the strain calculations through an inverse distance weighting algorithm [40]. The inverse distance weighting was followed by an additional median filter with a  $3 \times 3 \times 3$  stencil to filter out large local displacements in individual nodes. The latter addresses converged, yet unreliable data points, in the dataset and was considered as a trade-off arising from the somewhat small subwindow size that lead to higher uncertainties in the calculated displacement field. An illustration of the displacement field before and after filtering is shown in Fig. A.11.

#### References

- [1] B. Bell, European railway bridge problems: Sustainable bridges SB-D1.3, 2004, URL: <http://urn.kb.se/resolve?urn=urn:nbn:se:ltu:diva-74995>.
- [2] L. Bertolini, B. Elsener, P. Pedferri, E. Redaelli, R. Polder, Corrosion of Steel in Concrete: Prevention, Diagnosis, Repair, second ed., John Wiley & Sons, Weinheim, 2014, <http://dx.doi.org/10.1002/3527603379>, Incorporated.
- [3] E. Chen, C.G. Berrocal, I. Fernandez, I. Löfgren, K. Lundgren, Assessment of the mechanical behaviour of reinforcement bars with localised pitting corrosion by digital image correlation, Eng. Struct. 219 (2020) 110936, <http://dx.doi.org/10.1016/j.engstruct.2020.110936>.
- [4] W. Zhang, X. Song, X. Gu, S. Li, Tensile and fatigue performance of corroded rebars, Constr. Build. Mater. 34 (2012) 409–417, <http://dx.doi.org/10.1016/j.conbuildmat.2012.02.071>.
- [5] M. Mak, P. Desnerck, J. Lees, Corrosion-induced cracking and bond strength in reinforced concrete, Constr. Build. Mater. 208 (2019) 228–241, <http://dx.doi.org/10.1016/j.conbuildmat.2019.02.151>.
- [6] A. Michel, B.J. Pease, M.R. Geiker, H. Stang, J.F. Olesen, Monitoring reinforcement corrosion and corrosion-induced cracking using non-destructive x-ray attenuation measurements, Cem. Concr. Res. 41 (2011) 1085–1094, <http://dx.doi.org/10.1016/j.cemconres.2011.06.006>.
- [7] E. Sola, J. Ožolt, G. Balabanić, Z. Mir, Experimental and numerical study of accelerated corrosion of steel reinforcement in concrete: Transport of corrosion products, Cem. Concr. Res. 120 (2019) 119–131, <http://dx.doi.org/10.1016/j.cemconres.2019.03.018>.
- [8] K. Tuutti, Corrosion of Steel in Concrete, Swedish Cement and Concrete Research Institute, Stockholm, 1982, URL: <http://www.cbi.se/viewNavMenu.do?menuID=317&oid=857>.
- [9] C. Andrade, C. Alonso, F.J. Molina, Cover cracking as a function of bar corrosion: Part I-Experimental test, Mater. Struct. 26 (1993) 453–464, <http://dx.doi.org/10.1007/BF02472805>.
- [10] J.G. Cabrera, Deterioration of concrete due to reinforcement steel corrosion, Cem. Concr. Compos. 18 (1996) 47–59, [http://dx.doi.org/10.1016/0958-9465\(95\)00043-7](http://dx.doi.org/10.1016/0958-9465(95)00043-7).
- [11] C. Alonso, C. Andrade, J. Rodríguez, J.M. Díez, Factors controlling cracking of concrete affected by reinforcement corrosion, Mater. Struct./Mater. Constr. 31 (1998) 435–441, <http://dx.doi.org/10.1007/bf02480466>.

- [12] C. Andrade, A. Cesetti, G. Mancini, F. Tondolo, Estimating corrosion attack in reinforced concrete by means of crack opening, *Struct. Concr.* 17 (2016) 533–540, <http://dx.doi.org/10.1002/suco.201500114>.
- [13] F.U.A. Shaikh, Effect of cracking on corrosion of steel in concrete, *Int. J. Concr. Struct. Mater.* 12 (2018) <http://dx.doi.org/10.1186/s40069-018-0234-y>.
- [14] E. Chen, C.G. Berrocal, I. Lögren, K. Lundgren, Correlation between concrete cracks and corrosion characteristics of steel reinforcement in pre-cracked plain and fibre-reinforced concrete beams, *Mater. Struct./Mater. Constr.* 53 (2020) 1–22, <http://dx.doi.org/10.1617/s11527-020-01466-z>.
- [15] M. Tahershamsi, I. Fernandez, K. Lundgren, K. Zandi, Investigating correlations between crack width, corrosion level and anchorage capacity, *Struct. Infrastr. Eng.* 13 (2017) 1294–1307, <http://dx.doi.org/10.1080/15732479.2016.1263673>.
- [16] C.G. Berrocal, I. Fernandez, R. Rempling, The interplay between corrosion and cracks in reinforced concrete beams with non-uniform reinforcement corrosion, *Mater. Struct./Mater. Constr.* 55 (2022) <http://dx.doi.org/10.1617/s11527-022-01956-2>.
- [17] Z.P. Baž, Physical model for steel corrosion in concrete sea structures - application, *J. Struct. Div.* 105 (1979) <http://dx.doi.org/10.1061/JSDEAG.0005169>.
- [18] Y. Liu, R.E. Weyers, Modeling the time-to-corrosion cracking in chloride contaminated reinforced concrete structures, *ACI Mater. J.* 95 (1998) 675–681, <http://dx.doi.org/10.14359/410>.
- [19] K. Lundgren, Modelling the effect of corrosion on bond in reinforced concrete, *Mag. Concr. Res.* 54 (2002) 165–173, <http://dx.doi.org/10.1680/macr.54.3.165.38798>.
- [20] J. Özolt, F. Oršanić, G. Balabanić, M. Kušter, Modeling damage in concrete caused by corrosion of reinforcement: Coupled 3D FE model, *Int. J. Fract.* 178 (2012) 233–244, <http://dx.doi.org/10.1007/s10704-012-9774-3>.
- [21] B. Švija, M. Luković, J. Pacheco, E. Schlangen, Cracking of the concrete cover due to reinforcement corrosion: A two-dimensional lattice model study, *Constr. Build. Mater.* 44 (2013) 626–638, <http://dx.doi.org/10.1016/j.conbuildmat.2013.03.063>.
- [22] C. Fahy, S.J. Wheeler, D. Gallipoli, P. Grassl, Corrosion induced cracking modelled by a coupled transport-structural approach, *Cem. Concr. Res.* 94 (2017) 24–35, <http://dx.doi.org/10.1016/j.cemconres.2017.01.007>.
- [23] W. Hwang, K. Yong Ann, Determination of rust formation to cracking at the steel-concrete interface by corrosion of steel in concrete, *Constr. Build. Mater.* 367 (2023) <http://dx.doi.org/10.1016/j.conbuildmat.2022.130215>.
- [24] P. Zhang, P. Wang, D. Hou, Z. Liu, M. Haist, T. Zhao, Application of neutron radiography in observing and quantifying the time-dependent moisture distributions in multi-cracked cement-based composites, *Cem. Concr. Compos.* 78 (2017) 13–20, <http://dx.doi.org/10.1016/j.cemconcomp.2016.12.006>.
- [25] H. Sun, D. Zhao, Y. Gu, S. Memon, Z. Ren, B. Liu, X. Zhang, F. Xing, D. Li, Three-dimensional characterization of steel corrosion embedded in cement paste, *Constr. Build. Mater.* 143 (2017) 24–32, <http://dx.doi.org/10.1016/j.conbuildmat.2017.03.106>.
- [26] B. Dong, G. Fang, Y. Liu, P. Dong, J. Zhang, F. Xing, S. Hong, Monitoring reinforcement corrosion and corrosion-induced cracking by X-ray microcomputed tomography method, *Cem. Concr. Res.* 100 (2017) 311–321, <http://dx.doi.org/10.1016/j.cemconres.2017.07.009>.
- [27] S. Brisard, M. Serdar, P. Monteiro, Multiscale X-ray tomography of cementitious materials: A review, *Cem. Concr. Res.* 128 (2020) <http://dx.doi.org/10.1016/j.cemconres.2019.105824>.
- [28] A. Tengattini, N. Lenoir, E. Andò, G. Viggiani, Neutron imaging for geoscience: A review, *Geomech. Energy Environ.* 27 (2021) 100206, <http://dx.doi.org/10.1016/j.gete.2020.100206>.
- [29] S. Robuschi, A. Tengattini, J. Dijkstra, K. Lundgren, A closer look at corrosion of steel reinforcement bars in concrete using 3D neutron and X-ray computed tomography, *Cem. Concr. Res.* 148 (2021) 106439, <http://dx.doi.org/10.1016/j.cemconres.2021.106439>.
- [30] A. Boschmann Kä, Chloride-Induced Reinforcement Corrosion in Concrete: The Role of the Steel-Concrete Interface and Implications for Engineering (Doctoral Thesis Nr. 26213), ETH Zurich, 2019, <http://dx.doi.org/10.3929/ethz-b-000403511>.
- [31] S. Robuschi, K. Lundgren, I. Fernandez, M. Flansbjerg, Anchorage of naturally corroded, plain reinforcement bars in flexural members, *Mater. Struct.* 53 (2020) 38, <http://dx.doi.org/10.1617/s11527-020-01471-2>.
- [32] Creaform, Handyscan 3D SILVER series, 2022, URL: <https://www.creaform3d.com/en/handyscan-3d-silver-series-professional-3d>.
- [33] Cement - Part 1: Composition, Specifications and Conformity Criteria for Common Cements, EN 197-1, Comité Européen de Normalisation (CEN), Europe, 2011.
- [34] Testing Hardened Concrete - Part 3: Compressive Strength of Test Specimens, EN 12390-3, Comité Européen de Normalisation (CEN), Europe, 2019.
- [35] R.T. 187-SOC, Experimental Determination of the Stress-Crack Opening: Final Report, RILEM, RILEM Publ., Bagneux, 2007.
- [36] G. Mancini, F. Tondolo, Effect of bond degradation due to corrosion - a literature study, *Struct. Concr.* 15 (2014) 408–418, <http://dx.doi.org/10.1002/suco.201300009>.
- [37] A. Tengattini, N. Lenoir, E. Andò, B. Giroud, D. Atkins, J. Beaucour, G. Viggiani, NeXT-grenoble, the neutron and X-ray tomograph in grenoble, *Nucl. Instrum. Methods Phys. Res. Sect. A* 968 (2020) 163939, <http://dx.doi.org/10.1016/j.nima.2020.163939>.
- [38] L. Feldkamp, L. Davis, J. Kress, Practical cone-beam algorithm, *J. Opt. Soc. Amer.* 1 (6) (1984) 612–619.
- [39] F. Maes, A. Collignon, D. Vandermeulen, G. Marchal, P. Suetens, Multimodality image registration by maximization of mutual information, *IEEE Trans. Med. Imaging* 16 (1997) 187–198, <http://dx.doi.org/10.1109/42.563664>.
- [40] O. Stamati, et al., Spam: Software for practical analysis of materials, *J. Open Source Softw.* 5 (51) (2022) 2286, <http://dx.doi.org/10.21105/joss.02286>.
- [41] P. Santiago, D. Gage, Statistical models of partial volume effect, *IEEE Trans. Image Process.* 4 (1995) 1531–1540, <http://dx.doi.org/10.1109/83.469934>.
- [42] R. Ketcham, R. Hanna, Beam hardening correction for X-ray computed tomography of heterogeneous natural materials, *Comput. Geosci.* 67 (2014) 49–61, <http://dx.doi.org/10.1016/j.cageo.2014.03.003>.
- [43] S. Hong, G. Shi, F. Zheng, M. Liu, D. Hou, B. Dong, Characterization of the corrosion profiles of reinforcement with different impressed current densities by X-ray micro-computed tomography, *Cem. Concr. Compos.* 109 (2020) 103583, <http://dx.doi.org/10.1016/j.cemconcomp.2020.103583>.
- [44] G. Fang, W. Ding, Y. Liu, J. Zhang, F. Xing, B. Dong, Identification of corrosion products and 3D distribution in reinforced concrete using X-ray micro computed tomography, *Constr. Build. Mater.* 207 (2019) 304–315, <http://dx.doi.org/10.1016/j.conbuildmat.2019.02.133>.
- [45] H. Sun, C. Jiang, K. Cao, D. Yu, W. Liu, X. Zhang, F. Xing, D. Zhao, Monitoring of steel corrosion and cracking in cement paste exposed to combined sulfate-chloride attack with X-ray microtomography, *Constr. Build. Mater.* 302 (2021) <http://dx.doi.org/10.1016/j.conbuildmat.2021.124345>.
- [46] Y. Zhao, H. Dai, H. Ren, W. Jin, Experimental study of the modulus of steel corrosion in a concrete port, *Corros. Sci.* 56 (2012) 17–25, <http://dx.doi.org/10.1016/j.corsci.2011.11.004>.